The Cryosphere Discuss., 7, 4287–4319, 2013
www.the-cryosphere-discuss.net/7/4287/2013/
doi:10.5194/tcd-7-4287-2013

The Cryosphere Discussions
Open Access

A range correction for ICESat and its potential impact on ice sheet mass balance studies

A. A. Borsa[1], **G. Moholdt**[1], **H. A. Fricker**[1], **and K. M. Brunt**[2,3]

[1]Scripps Institution of Oceanography, San Diego, California, USA
[2]Morgan State University, Baltimore, Maryland, USA
[3]GESTAR, NASA Goddard Space Flight Center, Greenbelt, Maryland, USA

Received: 25 July 2013 – Accepted: 30 July 2013 – Published: 30 August 2013

Correspondence to: A. A. Borsa (aborsa@ucsd.edu)

Published by Copernicus Publications on behalf of the European Geosciences Union.

Abstract

We report on a range error in NASA's Ice, Cloud and land Elevation Satellite (ICESat) that degrades elevation precision and introduces a small but significant elevation trend over the ICESat mission period. This range error (the Gaussian-Centroid or "G-C" offset) varies on a shot-to-shot basis and increases in magnitude as laser transmit energies decline. Although the G-C offset is uncorrelated over periods ≤ 1 day, it evolves over the life of each of ICESat's three lasers in a series of ramps and jumps that give rise to spurious elevation trends of 0.92 to 1.90 cm yr^{-1}, depending on the time period considered. Using data over the Ross and Filchner-Ronne ice shelves we show that (1) the G-C offset introduces significant biases in ice-shelf mass balance estimates, and (2) the mass balance bias can vary between regions because of different temporal sampling of ICESat. We can accurately reproduce the impact of the G-C offset on these two ice shelves by fitting trends to sample-weighted global mean G-C offsets for each campaign, suggesting that it may not be necessary to fully repeat earlier ICESat studies to determine the impact of the G-C offset on ice sheet mass balance estimates.

1 Introduction

NASA's Ice, Cloud, and land Elevation Satellite (ICESat) (Schutz et al., 2005) was an Earth-orbiting laser altimeter mission that operated from 2003–2009. ICESat's primary task was to repeatedly measure the elevations of Earth's ice sheets to help quantify their contribution to sea level change in response to increasing atmospheric and ocean temperatures. Many studies have used ICESat elevation data to quantify volume/mass changes of glaciers (e.g., Gardner et al., 2013), ice shelves (e.g., Pritchard et al., 2012), and ice sheets (e.g., Shepherd et al., 2012), and ICESat data have been combined with other measurements to increase the spatiotemporal coverage and resolution of surface change estimates. These complementary data include airborne laser altimetry from NASA's Operation IceBridge mission (Koenig, et al., 2010; Kwok et al., 2012;

TCD
7, 4287–4319, 2013

Schenk and Csathó, 2012), gravity from the NASA/DLR GRACE mission (Riva et al., 2009), and elevations from ESA's ERS-1, ERS-2 and Envisat radar altimeters (Zwally et al., 2011; Hurkmans et al., 2012). ICESat will provide benchmark elevations for the planned ICESat-2 mission (Abdalati et al., 2010), which would extend the satellite laser altimeter record to 15 yr or more.

Since the ice sheets are so vast, a 1 cm elevation change over all grounded ice corresponds to a mass change of 134 Gt and a sea-level equivalent of 0.37 mm. Centimeter-level systematic errors in satellite altimeter measurements are therefore crucial to ice mass balance estimates, and ICESat underwent rigorous calibration and validation to ensure that it would meet its accuracy target of 2 cm yr^{-1} elevation change averaged over 100 × 100 km regions (Zwally et al., 2002). The ICESat calibration program was based on the minimization of elevation residuals from regularly-repeated pointing maneuvers over the open ocean (e.g., Luthcke et al., 2005), with subsidiary efforts to help calibrate timing and geolocation (Magruder et al., 2007, 2010) and to mitigate the impact of detector saturation (Fricker et al., 2005). ICESat validation included crossover analysis to determine ICESat's initial precision and accuracy (Shuman et al., 2006; Brenner et al., 2007), followed by long-term elevation comparisons with respect to stable and/or independently-characterized reference surfaces (Fricker et al., 2005; Urban and Schutz, 2005; Borsa et al., 2007, 2008; Shuman et al., 2009).

Although ICESat was intended to be operated continuously throughout its mission (Abshire et al., 2003), laser reliability concerns after the failure of the first ICESat laser led to it being operated "campaign-style" – whereby data were acquired in a series of ~ 33-day campaigns spaced 4–6 months apart (Table 1). The ICESat validation effort focused largely on documenting changes in ICESat elevation accuracy from campaign to campaign and between different releases of ICESat data (e.g., Fricker et al., 2005). Despite ongoing refinements in elevation retrieval (reflected in higher product release numbers), multiple studies have documented persistent instrument-related elevation biases between campaigns (Gunter et al., 2009; Riva et al., 2009; Siegfried et al., 2011). More importantly, these "inter-campaign biases" exhibit statistically significant (albeit

TCD
7, 4287–4319, 2013

different) trends over the ICESat mission period (Urban et al., 2012). Furthermore, researchers estimating ice mass balance using ICESat data have taken different approaches with respect to inter-campaign biases, with some choosing not to correct for them (Pritchard et al., 2009; Gardner et al., 2013) and others applying biases from one of several sources (Gunter et al., 2009; Riva et al., 2009; Zwally et al., 2011; Shepherd et al., 2012).

This paper describes a previously unrecognized component of the ICESat inter-campaign biases, an inadvertent range error (called the Gaussian-Centroid or "G-C" offset) that was introduced during the processing of Level 1 data. Correcting for this error improves the precision of individual elevation measurements and removes a small but significant anomalous elevation trend from ICESat data. Using global statistics for the G-C offset and case studies over a terrestrial reference surface and two Antarctic ice shelves, we demonstrate the potential impact that the correction has on elevation accuracy and ice sheet mass balance.

2 Data and analysis

2.1 ICESat campaigns

Data collection during the ICESat mission took place during 18 separate campaigns between February 2003 and October 2009 (Table 1). In this paper, we refer to these campaigns using the standard convention of pairing the number of the operational laser with a letter designating each consecutive campaign for that laser (e.g., L2a is the first campaign for Laser 2, L3b is the second campaign for Laser 3, etc.). Laser 1 operated for only 56 days before it failed and thus was flown only in ICESat's 8-day exact-repeat calibration orbit. Most published studies use data from L2a onwards (after the spacecraft had transitioned to its 91-day repeat orbit) so we will focus primarily on Lasers 2 and 3. To avoid confusion about the time sequence of the laser campaigns, we

TCD
7, 4287–4319, 2013

note that Laser 2 was switched off after L2c and then back on again after Laser 3 failed, which is why campaigns L2d–L2f took place after L3k (the final Laser 3 campaign).

2.2 ICESat elevation validation at the salar de Uyuni

This study arose from our ICESat validation work involving elevation comparisons with a GPS-derived reference DEM acquired several months before launch at the salar de Uyuni in Bolivia (Fig. 1) (Fricker et al., 2005; Borsa et al., 2007). Total topographic relief over the 45-by-54 km Uyuni DEM is only 80 cm, making this one of the flattest surfaces on Earth. Both ascending (Track 360) and descending (Track 85) ICESat tracks cross the Uyuni DEM, and over 300 individual laser footprints from each track fall within the DEM boundaries. In 2009, we resurveyed the salar de Uyuni to check for topographic change that might impact ICESat elevation validation and found that the DEM surface had risen by an average of 2.5 cm (Brunt et al., 2009). For the analysis used in this paper, we mitigate the effects of this surface change by linearly interpolating in time between the 2002 and 2009 DEMs to the date of each ICESat pass over the salar, creating a unique hybrid reference DEM for each track in each campaign.

At the salar de Uyuni, inter-campaign biases for the latest release of the ICESat data (R633) range over 10 cm, with elevation biases of up to 17 cm between repeated tracks within a single campaign (see Fricker et al. (2005) for a summary of our methods). These values are of similar magnitude to what has been observed by other investigators in different locations (Shuman et al., 2009; Siegfried et al., 2011; Urban et al. 2012). The salar de Uyuni is an ideal validation site – high-elevation (smaller hydrostatic delay correction) with negligible cloud cover (little or no multiple scattering) and no topography (little or no elevation impact from pointing errors) – so we expected more accurate elevation recovery than we observed. At the same time we realized that with such a large range of observed biases, we had an opportunity to use the salar de Uyuni for calibration rather than just validation and could potentially uncover candidates for the unidentified error sources affecting ICESat elevations.

TCD
7, 4287–4319, 2013

2.3 Correlations between transmit pulse parameters and ICESat elevations

For this study, we undertook a systematic examination of the elevation impact of a number of ICESat metadata parameters, motivated by observations made by our group and other investigators that some of these parameters varied systematically from campaign to campaign (e.g., Fricker et al., 2005; Shuman et al. 2009). We hypothesized that at the salar de Uyuni we would be able to observe correlations between these parameters and the elevation biases remaining despite improvements in ICESat orbit determination, pointing, and ranging over the life of the mission (see http://nsidc.org/data/icesat/past_releases.html). Although we recorded and tracked instrument and environmental metadata as part of our validation activities, we had not previously looked for quantitative correlations between these metadata and the ICESat elevation biases over Uyuni.

In order to maximize the number of independent data in our analysis, we did not work with inter-campaign biases, but instead used the individual elevation misfits (the differences between the ICESat and interpolated DEM elevations) for all 8371 valid ICESat returns over the salar de Uyuni DEM. We regressed these misfits against a number of metadata parameters, including (1) transmit pulse skewness, (2) transmit pulse eccentricity, (3) transmit gain, (4) transmit pulse energy, and (5) receive pulse energy. We highlight these parameters because they all exhibit some degree of correlation with footprint elevation misfits. In the case of transmit pulse skewness, visual examination of the scatterplot between skewness and misfit (Fig. 2) shows that the two are linearly correlated, with stronger correlations for individual campaigns than for the entire dataset. Quantitatively, the linear Pearson correlation coefficient R between skewness and misfit is 0.30 (and statistically significant) for the entire dataset, with values for individual campaigns that reach 0.64 for L2b and L3c. Since parameters 1–2 are related to the transmit pulse shape and parameters 3–5 are directly or indirectly related to transmit pulse amplitude, we concluded that characteristics of the transmit pulse were affecting ICESat range determination and were able to identify a potential

TCD
7, 4287–4319, 2013

mechanism for this effect in the ICESat Range Algorithm Theoretical Basis Document (ATBD) (Brenner et al., 2003).

ICESat's transmit and return pulses are recorded as waveforms of energy versus time, with each waveform sample spanning 1 ns (equivalent to 15 cm in range). ICESat Level 1 data post-processing identifies the times associated with reference points on the transmit and return waveforms and differences the two to obtain the pulse travel time. Both reference points should refer to a common place on both waveforms to avoid biasing the travel time measurement, however a figure in the ICESat Range ATBD specified two different types of reference point: the *centroid* of the transmit waveform and the *peak position of the Gaussian fit* to the return waveform (Fig. 3). If the ATBD figure were correct, any deviation of the transmit waveform shape from a perfect Gaussian would cause a divergence between the centroids and Gaussian peaks of both the transmit and return waveforms. The result would be a timing/range error that would propagate through the geolocation process to yield a corresponding elevation error of similar magnitude but opposite sign.

2.4 An ICESat range error: the Gaussian-Centroid (G-C) offset

Although Gaussian-to-centroid (or G-C) timing was not intended to be used for range determination for simple ICESat return waveforms (D. Yi, personal communication, 2012), NASA's ICESat Science Computing Facility confirmed that G-C timing was implemented through data release R633 for all ICESat products except GLA14 (land/canopy elevations). Fortunately, the range error due to G-C timing can be reproduced exactly using the transmit pulse parameters available in the ICESat GLA05 data product (see http://nsidc.org/data/icesat/data.html).

The G-C range error (henceforth the "G-C offset") can be calculated as

$$\text{G-C offset(m)} = (\text{GLA05.d\_parmTr(2)} - \text{GLA05.d\_locTr}) \cdot c \quad (1)$$

where d_locTr is the GLA05 parameter containing the time (in ns) corresponding to the transmit waveform centroid, d_parmTr(2) is the GLA05 parameter containing the

TCD
7, 4287–4319, 2013

time (in ns) of the peak of the Gaussian fit to the transmit waveform, and the speed of light c is defined as $0.150\,\mathrm{m\,ns^{-1}}$. The elevation impact of the G-C offset can be removed by adding the offset from Eq. (1) directly to ICESat elevations, a step we refer to as the "G-C correction" in Sect. 3 below. Alternatively, investigators can apply the G-C correction from files provided by the National Snow and Ice Data Center (http://nsidc.org/data/icesat/correction-to-product-surface-elevations.html). Technically, the G-C offset/correction should also be scaled by the cosine of the laser pointing angle measured from nadir, but since this angle is rarely over 3 degrees, the scaling is < 1 mm and is negligible in most cases.

2.5 G-C offset characteristics for ICESat's three lasers

We took the entire ICESat dataset and used Eq. (1) to calculate the G-C offset for all laser pulses with a valid surface return. Ordering the pulses sequentially by laser shot, we found significant and systematic differences in the G-C offset between the three lasers and over the life of each laser (Fig. 4; Table 1).

During its short life, Laser 1 had a mean G-C offset of 1.77 cm, a G-C offset standard deviation of 1.99 cm, and little change in G-C offset behavior over time (Fig. 4a). Laser 2 had almost the same mean offset as Laser 1 (1.76 cm), but more than double the offset standard deviation (4.80 cm; Fig. 4b). Laser 2 also exhibited a four-fold increase in G-C offset standard deviation from L2c to L2f, which was associated with low (sub-20 mJ) and declining transmit energies. Increased variance is expected with low transmit energy because the accompanying decrease in the signal-to-noise ratio of the laser waveforms (once the transmit gain can no longer be increased to compensate) degrades the precision of centroid determination and Gaussian fitting (Fricker et al., 2005). In addition, there were significant changes in the moving average of the G-C offset (the red line in Fig. 4a), including (1) a 5 cm drop at the end of L2a that is associated with an instantaneous 10 mJ fall in transmit power and is probably due to the failure of one of the diode pump bars, (2) a large negative spike at the beginning of L2b during the period ICESat was in sun acquisition mode, and (3) an inverse correlation

TCD
7, 4287–4319, 2013

with transmit power beginning in L2d, which was when transmit energy fell and stayed below 10 mJ.

By contrast, Laser 3 showed much more stable G-C offset behavior, due in part to its higher transmit energies (Fig. 4c). Overall, Laser 3 had a lower mean G-C offset value than the other two lasers (−3.38 cm) and a relatively constant standard deviation whose value was close to that of Laser 1 (2.32 cm). The Laser 3 offset moving average started around 0 cm, jumped 3 cm in the middle of L3a (when the laser temperature was increased from 13.8 to 16.0 °C), and then gradually dropped by 4 cm through L3d and showed little change afterwards.

3 Results and discussion

3.1 Trend in the G-C offset over the ICESat mission

There are two direct effects of the G-C offset: (1) it increases the shot-to-shot variability of ICESat elevations (especially at low transmit energies) and (2) it shifts the mean elevation for most campaigns. Of greater relevance to ice sheet mass balance studies is a secondary effect due to the fact that when ordered in time, the changes in the mean G-C offset between campaigns exhibit a trend over the mission period (Fig. 5) that could potentially be interpreted as real surface elevation change ($\mathrm{d}h/\mathrm{d}t$).

We estimated the G-C offset trend via a linear regression against time of the global mean G-C offsets for campaigns L2a to L2f, with inverse-variance weights for each campaign calculated from the offset standard deviations (all data are from Table 1). This choice of weighting lowers the contribution of high-variance data points, which in this case are the three Laser 2 campaigns at the end of the mission. For the L2a–L2f period, we obtained a trend of $-1.38 \pm 0.40\,\mathrm{cm\,yr^{-1}}$, which is statistically different from zero at the 3-sigma level. Since many published studies do not include the later ICESat campaigns in their analysis, we also report trends for other data periods (Table 2, Trend A). As Table 2 and Fig. 5 show, the fewer campaigns used at the end of the ICESat

TCD
7, 4287–4319, 2013

mission, the more negative the trend of the G-C offset: up to $-2.13 \pm 0.53\,\mathrm{cm\,yr^{-1}}$ in the case of data spanning only the period between L2a to L3i.

3.2 Potential impact of the G-C offset on ICESat elevation trends

The negative trend in the G-C offset contributes an erroneous positive trend in ICESat elevations that could be interpreted as real surface change. However, the trends we calculated in Sect. 3.1 may not reflect the actual effect of the G-C offset on ICESat-derived dh/dt in cases that involve different regression weighting, as we discuss below.

ICESat investigators estimate volume change by integrating many independent dh/dt estimates over a region of interest. If ICESat elevation data are not corrected for the G-C offset, the offset will propagate through the linear regression used to obtain the dh/dt estimates and introduce a trend error that depends on the weighting applied to the elevations (see Appendix A). Most investigators use constant weighting for all returns (e.g., Shepherd et al., 2012), so we repeated the linear regressions from Sect. 3.1 using a uniform weight on each campaign of $1/4\,\mathrm{cm^{-2}}$ (corresponding to a 2.0 cm standard deviation) to see how this would change the G-C offset trend. The result was less negative trend estimates (Table 2, Trend B), with the biggest change for the longest data periods (e.g., for L2a–L2e and L2a–L2f). Using a different value for the uniform weight will not change the trend estimates, although it will change the formal error obtained for those trends.

The number of ICESat measurements in each campaign (i.e. sampling) also affects how the G-C offset will affect dh/dt estimates. For example, campaign L2f has fewer returns than any of the other campaigns because it was only 11 days long and because its low laser transmit energy resulted in a low percentage of valid returns being recorded due to attenuation by clouds. There are relatively few L2f elevations included in the many thousands of dh/dt estimates made over an ice sheet, which means that L2f elevations (and therefore the G-C offset for L2f) are typically underweighted in the average ice sheet dh/dt.

TCD
7, 4287–4319, 2013

We can estimate the impact of sampling density on the G-C trend by modifying the uniform-variance regression weights above to include a term for number of returns expected for each campaign on a global basis (Appendix A). The resulting trend estimates (Table 2, Trend C) are more negative than they would be if sampling density were not considered. This is due to the lower weighting of the sparse L2d, L2e and L2f campaigns, whose relatively high G-C offsets now have a smaller impact on the G-C trend estimate. These trends are our best approximation of the impact of removing the G-C offset from ICESat elevations, although differences in relative ICESat sampling from the global campaign averages (due to regional effects or data editing protocols) are likely to cause the dh/dt impact of the G-C offset in specific cases to vary from our estimates.

3.3 Power spectrum of the G-C offset

To determine whether there might be regional variation in the G-C offset, we examined the G-C offset power spectrum to look for temporal correlations that could map into spatial patterns. For this analysis we could not use G-C offsets calculated from the centroid and Gaussian parameters in the GLA05 data product, since shots without a valid return (see Table 1) did not undergo Gaussian fitting during ICESat data processing. Spectral estimation requires continuous time series, so we retrieved transmit waveform records from the GLA01 data product, estimated Gaussian fits for every ICESat transmit pulse, and recalculated the G-C offset using Eq. (1) and the original GLA05 centroids. The new G-C offsets deviate from the GLA05-derived offsets by 0.0 ± 2.5 mm (1-sigma) overall and are continuous over each campaign.

We calculated G-C offset power spectral density (PSD) estimates for each of the 18 ICESat campaigns using a single-window Fast Fourier Transform (FFT) with a Hamming taper. In all cases, the PSDs follow the same pattern: a flat spectrum at frequencies higher than about 10^{-5} Hz and, if there were any jumps or ramps in the G-C offset time series during the campaign, a fractal spectrum with spectral slopes ranging from 0 to −2 at frequencies lower than 10^{-5} Hz (Fig. 4). What these results show is that the

TCD
7, 4287–4319, 2013

G-C offset behaves like white noise over periods shorter than a day, which implies negligible along-track structure over distances less than about 15 full orbits. Furthermore, because of the spatio-temporal pattern of ICESat tracks – whereby later tracks fill in between earlier tracks – changes in the G-C offset are almost uniformly distributed over a broad area such as an ice sheet. The global characteristics of the G-C offset should thus be a good first approximation to how the offset behaves in any regional analysis.

3.4 Impact of the G-C Offset on ICESat measurements of ice shelf d*h*/d*t*

In order to test our assumptions about the impact of the G-C offset on ICESat d*h*/d*t* estimates, we looked at two areas in Antarctica: the Ross and Filchner-Ronne ice shelves. For each ice shelf we estimated d*h*/d*t* for campaigns L2a–L2f using ICESat data with and without the G-C offset. (In the following discussion, we will use the term "G-C correction" to refer to the removal of the G-C offset by its addition to ICESat elevations). For this analysis, we followed the standard approach of simultaneously estimating planar slopes (d*h*/d*x*, d*h*/d*y*) and temporal trends (d*h*/d*t*) for nearby footprints along segments of ICESat near-repeat tracks using least-squares estimation with unit weighting (e.g., Smith et al., 2009; Gardner et al., 2013). We used saturation-corrected and tide-corrected elevations from the ICESat GLA12 data product, "retided" the elevations using a more accurate tide-model (Padman et al., 2002; Fricker and Padman, 2006), and estimated d*h*/d*t* only for reference tracks that contained four or more campaigns. Finally, for each ice shelf and method, we simply averaged all d*h*/d*t* estimates to derive a single d*h*/d*t* value without accounting for uneven spatial distribution (i.e. we did not interpolate estimates to a regular grid).

For the Ross Ice Shelf, the average d*h*/d*t* value changed by $-0.69\,\mathrm{cm\,yr^{-1}}$ after applying the G-C correction (from $+0.10\,\mathrm{cm\,yr^{-1}}$ to $-0.59\,\mathrm{cm\,yr^{-1}}$). For the Filchner-Ronne Ice Shelf, the average d*h*/d*t* value changed by $-0.48\,\mathrm{cm\,yr^{-1}}$ after applying the G-C correction (from $+1.80\,\mathrm{cm\,yr^{-1}}$ to $+1.32\,\mathrm{cm\,yr^{-1}}$). The reason the impact of the G-C correction is different for the two ice shelves is because the sampling of elevations from each campaign is different. Most relevant is the undersampling of the Filchner-Ronne

TCD
7, 4287–4319, 2013

Ice Shelf in L2a relative to the Ross Ice Shelf (see Table 3), which slightly flattens the G-C correction trend. This can be understood by observing that lowering the weight of L2a in Fig. 5 will tend to flatten the slope of the linear fit to the G-C offsets by mitigating the impact of the high L2a value. L3g and L3i are also sampled very differently on the two ice shelves, but they matter less because they are close to the center of the time series and because their mean G-C offset values are similar to those of nearby campaigns.

The G-C correction significantly changed the mass balance of the ice shelves we examined. Because of hydrostatic equilibrium, a given change in surface elevation equates to about nine times more change at the underside of the ice shelf, greatly magnifying the impact of systematic measurement errors. In the case of the Ross Ice Shelf, the $-0.69\,\mathrm{cm\,yr^{-1}}$ change in average dh/dt from the G-C correction implied a mass balance correction of $-29\,\mathrm{Gt\,yr^{-1}}$ after accounting for hydrostatic equilibrium. The mass balance correction for the Filchner-Ronne Ice Shelf from the change in average dh/dt was $-19\,\mathrm{Gt\,yr^{-1}}$.

In addition to the analysis described above, we also approximated the ice shelf elevation trend impact of the G-C correction using linear fits to the mean global G-C offsets of each campaign. For each ice shelf, we linearly regressed the mean G-C offsets from Table 1 against time, using the campaign sampling from Table 3 to derive appropriate weights via Eq. (A11) (Appendix A). We obtained estimates for the dh/dt impact of the G-C correction of $-0.61\,\mathrm{cm\,yr^{-1}}$ for the Ross Ice Shelf and $-0.49\,\mathrm{cm\,yr^{-1}}$ for the Filchner-Ronne Ice Shelf, both within $1\,\mathrm{mm\,yr^{-1}}$ of the actual dh/dt values calculated by applying the G-C correction and reprocessing the dataset. This suggests that it may not be necessary to fully repeat earlier ICESat studies to determine the impact of the G-C correction as long as the local sampling and explicit weighting scheme for each campaign is known.

TCD
7, 4287–4319, 2013

3.5 Relationship to estimates of inter-campaign biases

There have been many independent estimates made of ICESat inter-campaign biases, seven of which were presented by Urban et al. (2012). Importantly, there was almost no consensus amongst the authors who contributed to this presentation; indeed these seven estimates yielded biases that differed by up to 20 cm for any single campaign and bias trends that ranged from −0.3 to +2.2 cm yr^{-1} over the L2a–L2f period. Given the different surface types, data locations, spatial sampling, and methodologies used in these estimates, it is understandable that the implied biases might differ. However, since the inter-campaign bias trends (or their underlying biases) are supposed to be applied as corrections to all ICESat data, it is important to understand the reasons for and implications of the variability between the estimates.

For the purposes of this discussion, we can identify three components of the measured inter-campaign biases: (1) the contribution of the G-C offset, (2) bias due to all other instrument error sources, and (3) bias estimation errors due to actual elevation/range changes from unmodeled physical processes such as surface change and atmospheric scattering over the selected calibration surfaces. The contributions of all three components will vary according to the data and methodology used in the bias estimation. For instance, we demonstrated in Sect. 3.4 how the impact of the G-C offset differs by a few mm yr^{-1} between two ice shelves on the same continent because of data sampling. We might also expect, for example, differences between land-, ocean- and ice-determined biases due to systematic differences in cloud cover or surface geometry (e.g. sea-state effects). Larger differences are likely if biases are being estimated over surfaces that are assumed to be stable but are not, or over surfaces whose time variance is imperfectly known.

Applying the G-C correction removes the first component of the inter-campaign biases and thus will alter existing inter-campaign bias estimates. Specifically, we can expect the G-C correction to decrease inter-campaign bias trends by 0.92 to 1.90 cm yr^{-1} depending on the campaigns used (Table 2, Trend C). This means that the G-C offset is

TCD
7, 4287–4319, 2013

a significant contributor to the inter-campaign biases, although the large spread of the inter-campaign bias estimates indicates that significant residual variability will remain in all estimates after the G-C correction is implemented. Validation using the two ICESat tracks over the salar de Uyuni DEM (Fig. 1) confirms that the impact on the fitted elevation trend from applying the G-C correction to individual ICESat shots is almost the same as what we predict from the global analysis in Sect. 3.2 ($-0.92\,\mathrm{cm\,yr^{-1}}$ predicted versus $-1.17\,\mathrm{cm\,yr^{-1}}$ actual for L2a–L2f). The actual bias trend at Uyuni changed from $0.67 \pm 0.47\,\mathrm{cm\,yr^{-1}}$ to $-0.50 \pm 0.36\,\mathrm{cm\,yr^{-1}}$ after the G-C correction, with the non-zero residual trend illustrating the fact that some elevation error is likely to remain after the G-C offset is removed.

Of importance to previous studies that used ICESat data containing the G-C offset, recent studies have suggested (e.g., Rignot et al., 2013) that applying a set of inter-campaign biases implicitly corrects for the impact of the G-C offset, at least at the level of the mean elevation for each campaign. While technically true, we are concerned that this is not a satisfactory way to make the G-C correction. Applying empirical inter-campaign biases may correct the effect of the G-C offset, but the variability of inter-campaign biases from different sources suggests that this approach can introduce additional errors in dh/dt estimates. We suggest instead that investigators explicitly correct for the known G-C offset using one of the methods described in Sect. 2.4, with the understanding that characterizing the remaining elevation errors/biases will require additional work.

4 Conclusions and outlook

We propose a range correction to the ICESat Level 1 data that removes the effect of an erroneous travel time calculation in the Level 1 data (the G-C offset). The impact of the G-C offset on ice sheet elevation trends (dh/dt) can vary substantially depending on the time span of investigation and the data sampling in each observation campaign.

TCD
7, 4287–4319, 2013

If those factors are carefully considered, we have shown that it is possible to reproduce the effect of the G-C offset to within a few mm yr^{-1} at a regional scale.

Additional work is still needed to characterize the elevation errors that remain after the G-C offset is removed. This work includes the revision and ultimate reconciliation of various estimates of ICESat inter-campaign biases, all of which will change as a result of the G-C offset correction. The large variation in existing estimates of inter-campaign biases suggests that the problem of estimating empirical errors is not necessarily any easier than uncovering the root sources of those errors. We also wonder if the formalization of the inter-campaign bias as a description for otherwise unmodeled and persistent errors in ICESat elevations may have diverted attention away from the need for a more systematic and methodical effort to identify outstanding error sources in the ICESat data. In particular, we are concerned that a single "universal" set of inter-campaign biases (were one to become available) would not be equally relevant across a range of studies using different spatial subsets of data or different data sampling/editing.

The discovery of the G-C offset was the result of having access to a stable reference surface that allowed us to unambiguously link ICESat elevation anomalies to an ICESat timing error. Our approach can and should be applied to a broader sample of reference surfaces to provide a greater range of values for various instrument parameters, thereby increasing the diagnostic power of the correlation analysis. There are many active and potential reference sites around the globe, and we believe that the satellite altimetry community should attempt to link these into a single virtual surface for altimeter calibration and validation. Future missions might consider increasing both the resources and expectations for these efforts.

TCD
7, 4287–4319, 2013

Appendix A

Linear regression of mean G-C offsets to estimate the G-C impact on ICESat elevation trends

If we take the chi-square merit function for the linear fit to N pairs of time/elevation data

$$\chi^2(a,b) = \sum_{i=0}^{N-1} \left[\frac{(h_i + \Delta h_i) - (a + bt_i)}{\sigma_i} \right]^2 \quad \text{(A1)}$$

where the t_i are points in time corresponding to different ICESat campaigns, h_i are the "true" surface elevations, Δh_i are the corresponding G-C offsets, and σ_i are the standard deviations used for $(h_i + \Delta h_i)$, a linear regression will return the closed-form solution for the slope (or trend) b of the linear fit

$$b = \frac{\left[\sum_i \frac{1}{\sigma_i^2}\right]\left[\sum_i \frac{(h_i+\Delta h_i)t_i}{\sigma_i^2}\right] - \left[\sum_i \frac{t_i}{\sigma_i^2}\right]\left[\sum_i \frac{h_i+\Delta h_i}{\sigma_i^2}\right]}{\left[\sum_i \frac{1}{\sigma_i^2}\right]\left[\sum_i \frac{t_i^2}{\sigma_i^2}\right] - \left[\sum_i \frac{t_i}{\sigma_i^2}\right]^2}. \quad \text{(A2)}$$

Equation (A2) can be rewritten as

$$b = \frac{\left[\sum_i \frac{1}{\sigma_i^2}\right]\left[\sum_i \frac{h_i t_i}{\sigma_i^2}\right] - \left[\sum_i \frac{t_i}{\sigma_i^2}\right]\left[\sum_i \frac{h_i}{\sigma_i^2}\right]}{\left[\sum_i \frac{1}{\sigma_i^2}\right]\left[\sum_i \frac{t_i^2}{\sigma_i^2}\right] - \left[\sum_i \frac{t_i}{\sigma_i^2}\right]^2} + \frac{\left[\sum_i \frac{1}{\sigma_i^2}\right]\left[\sum_i \frac{\Delta h_i t_i}{\sigma_i^2}\right] - \left[\sum_i \frac{t_i}{\sigma_i^2}\right]\left[\sum_i \frac{\Delta h_i}{\sigma_i^2}\right]}{\left[\sum_i \frac{1}{\sigma_i^2}\right]\left[\sum_i \frac{t_i^2}{\sigma_i^2}\right] - \left[\sum_i \frac{t_i}{\sigma_i^2}\right]^2} \quad \text{(A3)}$$

which shows that the minimization of Eq. (A1) to find b is identical to the minimization of

$$\sum_{i=0}^{N-1} \left[\frac{h_i - (a + bt_i)}{\sigma_i} \right]^2 + \sum_{i=0}^{N-1} \left[\frac{\Delta h_i - (a + bt_i)}{\sigma_i} \right]^2 \quad \text{(A4)}$$

TCD
7, 4287–4319, 2013

or that

$$b = b_{surface} + b_{\text{G-C}}. \tag{A5}$$

The contribution of the G-C offset to the trend in the data can therefore be considered separately from the contribution of the surface elevations themselves, although the weighting will be the same in both cases.

To scale these conclusions from a single evaluation cell to an entire study area, we note that the ice volume change for a given region is calculated by summing the contribution of many independent trend estimates

$$\frac{\mathrm{d}V}{\mathrm{d}t} = \sum_j b_j A_j = \sum_j \left[b_{\text{surface}_j} + b_{G-C_j} \right] A_j = \sum_j b_{\text{surface}_j} A_j + \sum_j b_{G-C_j} A_j \tag{A6}$$

with separate terms for surface volume change and volume change from the G-C offset. If we make the simplifying assumption that the area A_j of each evaluation cell is the same (most studies interpolate volume/mass estimates to the nodes of a regular grid) and take M to be the number of cells, the second (G-C term) in Eq. (A6) can be written

$$\frac{\mathrm{d}V_{\text{G-C}}}{\mathrm{d}t} = A \sum_{j=0}^{M-1} b_{G-C_j} = MA \sum_{j=0}^{M-1} \frac{b_{G-C_j}}{M}. \tag{A7}$$

Substituting the linear regression solution for $b_{\text{G-C}}$ into Eq. (A7), taking the values for t_i and σ_i to be the same everywhere for a given campaign (although different between campaigns), and distributing the summation over j gives

TCD
7, 4287–4319, 2013

$$\frac{\mathrm{d}V_{\text{G-C}}}{\mathrm{d}t} = MA\sum_{j=0}^{M-1}\frac{1}{M}\left[\frac{\left[\sum_i \frac{1}{\sigma_i^2}\right]\left[\sum_i \frac{\Delta h_{ij} t_i}{\sigma_i^2}\right] - \left[\sum_i \frac{t_i}{\sigma_i^2}\right]\left[\sum_i \frac{\Delta h_{ij}}{\sigma_i^2}\right]}{\left[\sum_i \frac{1}{\sigma_i^2}\right]\left[\sum_i \frac{t_i^2}{\sigma_i^2}\right] - \left[\sum_i \frac{t_i}{\sigma_i^2}\right]^2}\right]$$

$$= MA\frac{\left[\sum_i \frac{1}{\sigma_i^2}\right]\left[\sum_i \frac{t_i}{\sigma_i^2}\sum_{j=0}^{M-1}\frac{\Delta h_{ij}}{M}\right] - \left[\sum_i \frac{t_i}{\sigma_i^2}\right]\left[\sum_i \frac{1}{\sigma_i^2}\sum_{j=0}^{M-1}\frac{\Delta h_{ij}}{M}\right]}{\left[\sum_i \frac{1}{\sigma_i^2}\right]\left[\sum_i \frac{t_i^2}{\sigma_i^2}\right] - \left[\sum_i \frac{t_i}{\sigma_i^2}\right]^2}$$

$$= MA\frac{\left[\sum_i \frac{1}{\sigma_i^2}\right]\left[\sum_i \frac{t_i}{\sigma_i^2}\Delta\bar{h}_i\right] - \left[\sum_i \frac{t_i}{\sigma_i^2}\right]\left[\sum_i \frac{1}{\sigma_i^2}\Delta\bar{h}_i\right]}{\left[\sum_i \frac{1}{\sigma_i^2}\right]\left[\sum_i \frac{t_i^2}{\sigma_i^2}\right] - \left[\sum_i \frac{t_i}{\sigma_i^2}\right]^2} \tag{A8}$$

where

$$\Delta\bar{h}_i = \sum_{j=0}^{M-1}\frac{\Delta h_{ij}}{M} \tag{A9}$$

is the average G-C offset value for the campaign indexed by i, and

$$\frac{\left[\sum_i \frac{1}{\sigma_i^2}\right]\left[\sum_i \frac{t_i}{\sigma_i^2}\Delta\bar{h}_i\right] - \left[\sum_i \frac{t_i}{\sigma_i^2}\right]\left[\sum_i \frac{1}{\sigma_i^2}\Delta\bar{h}_i\right]}{\left[\sum_i \frac{1}{\sigma_i^2}\right]\left[\sum_i \frac{t_i^2}{\sigma_i^2}\right] - \left[\sum_i \frac{t_i}{\sigma_i^2}\right]^2} \tag{A10}$$

is the estimate of the G-C offset trend from the mean G-C offsets.

TCD
7, 4287–4319, 2013

We have estimates of $\Delta\bar{h}_i$ from Table 1 (the mean G-C offset by campaign), which our analysis in Sect. 3.3 suggests should be valid anywhere on Earth. The conclusion from Eqs. (A8)–(A10) is that for uniform sampling of the various campaigns, estimating the impact of the G-C offset on ICESat elevation change trends only requires fitting a linear trend to a set of mean G-C offsets ordered in time, using whatever σ_i were chosen for the surface change analysis.

Finally, we consider the impact of sampling, whereby the number of valid ICESat returns can be different for different campaigns. In Eqs. (A3), (A4), this is manifested by having some campaigns with a large number of elevations/offsets and some with few (or even no) elevations/offsets, which implicitly down-weights campaigns with fewer samples. We would like to have a way of representing sampling when we fit linear trends to the G-C offset means in Eq. (A10). While it is beyond the scope of this paper to offer a proof, bootstrap analysis will confirm that a weighting that accounts for non-uniform sampling is

$$\sigma_i^2 = \frac{\sigma_i^2}{S_i} \frac{\sum S_i}{N} \tag{A11}$$

where the S_i are the number of samples for a given campaign in the study area and N is the total number of campaigns (as in Eq. A1). This formulation roughly preserves the value of the formal error on the slope estimate obtained from uniform-variance weighting. In the uniform-variance scenario typical for ICESat, what matters for the trend estimate is the relative number of samples between campaigns, not the absolute numbers.

Acknowledgements. The authors would like to acknowledge the valuable critique and feedback provided by Jay Zwally and his group at NASA's Goddard Space Flight Center on an earlier version of this manuscript. This work was supported by NASA's Research Opportunities in Space and Earth Sciences program under grant number NNX12AG67G.

TCD
7, 4287–4319, 2013

References

Abdalati, W., Zwally, H. J., Bindschadler, R., Csatho, B., Farrell, S., Fricker, H., Harding, D., Kwok, R., Lefsky, M., Markus, T., Marshak, A., Neumann, T., Palm, S., Schutz, B., Smith, B., Spinhirne, J., and Webb, C.: The ICESat-2 laser altimetry mission, Proceedings of the IEEE, 98, 5, 735–751, doi:10.1109/JPROC.2009.2034765, 2010.

Abshire, J. B., Sun, X., Riris, H., Sirota, M., McGarry, J., Palm, S., Ketchum, E. A., and Follas, R. B.: Geoscience Laser Altimeter System (GLAS) on the ICESat Mission: Pre-launch and on-orbit measurement performance, Geoscience and Remote Sensing Symposium, 2003, Proceedings, 21–25, July 2003.

Borsa, A. A., Minster, J. B., Bills, B. G., and Fricker, H. A.: Modeling long-period noise in kinematic GPS applications, J. Geodesy, 81, 157–170, doi:10.1007/s00190-006-0097-x, 2007.

Borsa, A. A., Fricker, H. A., Bills, B. G., Minster, J. B., Carabajal, C. C., and Quinn, K. J.: Topography of the salar de Uyuni, Bolivia from kinematic GPS, Geophys. J. Int., 172, 31–40, doi:10.1111/j.1365-246X.2007.03604.x, 2008.

Brenner, A. C., Zwally, H. J., Bentley, C. R., Csathó, B. M., Harding, D. J., Hofton, M. A., Minster, J.-B., Roberts, L. A. Saba, J. L., Thomas, R. H., and Yi., D.: Derivation of range and range distributions from laser pulse waveform analysis for surface elevations, roughness, slope, and vegetation heights, Algorithm Theoretical Basis Document, version 4.1 (available at: http://www.csr.utexas.edu/glas/atbd.html), Cent. for Space Res., Univ. of Tex., Austin, 2003.

Brenner, A. C., DiMarzio, J., and Zwally, H. J.: Precision and Accuracy of Satellite Radar and Laser Altimeter Data Over the Continental Ice Sheets, IEEE T. Geosci. Remote, 45, 321–331, doi:10.1109/TGRS.2006.887172, 2007.

Brunt, K. M., Borsa, A. A., and Fricker, H. A.: Repeated GPS surveys of the salar de Uyuni for continued calibration of ICESat altimeter data, Fall Meeting, AGU, San Francisco, CA, 14–18 December, 2009.

Fricker, H. A. and Padman, L.: Ice shelf grounding zone structure from ICESat laser altimetry, Geophys. Res. Lett., 33, L15502, doi:10.1029/2006GL026907, 2006.

Fricker, H. A., Borsa, A., Minster, B., Carabajal, C., Quinn, K., and Bill, B.: Assessment of ICESat performance at the salar de Uyuni, Bolivia, Geophys. Res. Lett., 32, L21S06, doi:10.1029/2005GL023423, 2005.

Gardner, A. S., Moholdt, G., Cogley, J. G., Wouters, B., Arendt, A. A., Wahr, J., Berthier, E., Hock, R., Pfeffer, W. T., Kaser, G., Ligtenberg, S. R. M., Bolch, T., Sharp, M. J., Hagen, J. O.,

TCD
7, 4287–4319, 2013

van den Broeke, M. R., and Paul, F.: A Reconciled Estimate of Glacier Contributions to Sea Level Rise: 2003 to 2009, Science, 340, 852–857, doi:10.1029/2011GL046583, 2013.
Gunter, B., Urban, T., Riva, R., Helsen, M., Harpold, R., Poole, S., Nagel, P., Schutz, B., and Tapley, B.: A comparison of coincident GRACE and ICESat data over Antarctica, J. Geodesy., 83, 1051–1060, doi:10.1007/s00190-009-0323-4, 2009.
Hurkmans, R. T. W. L., Bamber, J. L., and Griggs, J. A.: Brief communication "Importance of slope-induced error correction in volume change estimates from radar altimetry", The Cryosphere, 6, 447–451, doi:10.5194/tc-6-447-2012, 2012.
Koenig, L., Martin, S., Studinger, M., and Sonntag, J.: Polar Airborne Observations Fill Gap in Satellite Data, EOS Trans. AGU, 91, 38, 2010.
Kwok, R., Cunningham, G. F., Manizase, S. S., and Krabill, W. B.: Arctic sea ice freeboard from IceBridge acquisitions in 2009: Estimates and comparisons with ICESat, J. Geophys. Res., 117, C12013, doi:10.1029/2011JC007654, 2012.
Luthcke, S. B., Rowlands, D. D., Williams, T. A., and Sirota, M.: Reduction of ICESat systematic geolocation errors and the impact on ice sheet elevation change detection, Geophys. Res. Lett., 32, L21S05, doi:10.1029/2005GL023689, 2005.
Magruder, L. A., Webb, C. E., Urban, T. J., Silverberg, E. C., and Schutz, B. E.: ICESat altimetry data product verification at white sands space harbor, IEEE T. Geosci. Remote, 45, 147–155, doi:10.1109/TGRS.2006.885070, 2007.
Magruder, L. A., Ricklefs, R. L., Silverberg, E. C., Horstman, M. F., Suleman, M.A., and Schutz, B. E.: ICESat geolocation validation using airborne photography, IEEE T. Geosci. Remote, 48, 2758–2766, doi:10.1109/TGRS.2010.2040831, 2010.
Padman, L., Fricker, H. A., Coleman R., Howard S. L., and Erofeeva, S.: A new tide model for the Antarctic ice shelves and seas, Ann. Glaciol., 34, 247–254, 2002.
Pritchard, H. D., Arthern, R. J., Vaughan, D. G., and Edwards, L. A.: Extensive dynamic thinning on the margins of the Greenland and Antarctic ice sheets, Nature, 461, 971–975, doi:10.1038/nature08471, 2009.
Pritchard, H. D., Ligtenberg, S. R. M., Fricker, H. A., Vaughan, D. G., Van den Broeke, M. R., and Padman, L.: Antarctic ice-sheet loss driven by basal melting of ice shelves, Nature 484, 502–505, doi:10.1038/nature10968, 2012.
Rignot, E., Jacobs, S., Mouginot, J., and Scheuchl, B.: Ice shelf melting around Antarctic, Science, 341, 266–270, doi:10.1126/science.1235798, 2013.

TCD
7, 4287–4319, 2013

Riva, R. E. M., Gunter, B. C., Urban, T. J., Vermeersen, B. L. A., Lindenbergh, R. C., Helsen, M. M., Bamber, J. L., van de Wal, R. S. W., van den Broeke, M. R., and Schutz, B. E.: Glacial isostatic adjustment over Antarctica from combined ICESat and GRACE satellite data, Earth Planet. Sc. Lett., 288, 516–523, doi:10.1016/j.epsl.2009.10.013, 2009.

Schutz, B. E., Zwally, H. J., Shuman, C. A., Hancock, D., and DiMarzio, J. P.: Overview of the ICESat Mission, Geophys. Res. Lett., 32, L21S01, doi:10.1029/2005GL024009, 2005.

Shepherd, A., Ivins, E., A, G., Barletta, V., Bentley, M., Bettadpur, S., Briggs, K., Bromwich, D., Forsberg, R., Galin, N., Horwath, M., Jacobs, S., Joughin, I., King, M., Lenaerts, J., Li, J., Ligtenberg, S., Luckman, A., Luthcke, S., McMillan, M., Meister, R., Milne, G., Mouginot, J., Muir, A., Nicolas, J., Paden, J., Payne, A., Pritchard, H., Rignot, E., Rott, H., Sørensen, L., Scambos, T., Scheuchl, B., Schrama, E., Smith, B., Sundal, A., van Angelen, J., van de Berg, W., van den Broeke, M., Vaughan, D., Velicogna, I., Wahr, J., Whitehouse, P., Wingham, D., Yi, D., Young, D., and Zwally, H.: A reconciled estimate of ice-sheet mass balance, Science, 338, 1183–1189, doi:10.1126/science.1228102, 2012.

Schenk, T. and Csathó, B.: A New Methodology for Detecting Ice Sheet Surface Elevation Changes From Laser Altimetry Data, Geoscience and Remote Sensing, IEEE Transactions on, 50, 3302–3316, doi:10.1109/TGRS.2011.2182357, 2012.

Siegfried, M. R., Hawley, R. L., and Burkhart, J. F.: High-resolution ground-based GPS measurements show intercampaign bias in ICESat elevation data near Summit, Greenland, IEEE T. Geosci. Remote, 49, 3393–3400, doi:10.1109/TGRS.2011.2127483, 2011.

Shuman, C. A., Zwally, H. J., Schutz, B. E., Brenner, A. C., DiMarzio, J. P., Suchdeo, V. P., and Fricker, H. A.: ICESat Antarctic elevation data: preliminary precision and accuracy assessment, Geophys. Res. Lett., 33, L07501, doi:10.1029/2005GL025227, 2006.

Shuman, C. A., Harding, D. J., Dimarzio, J. P., Sun, X., Suchdeo, V. P., and Brenner, A.: Empirical correction of residual error in the ICESat-1 altimetry time series at Lake Vostok, Fall Meeting, AGU, San Francisco, CA, 14–18 December 2009.

Smith, B. E., Fricker, H. A., Joughin, I. R., and Tulaczyk, S.: An inventory of active subglacial lakes in Antarctica detected by ICESat (2003–2008), J. Glaciol., 55, 1 573–595, doi:10.3189/002214311795306682, 2009.

Urban, T. J. and Schutz, B. E.: ICESat sea level comparisons, Geophys. Res. Lett., 32, 23, doi:10.1029/2005GL024306, 2005.

Urban, T., Borsa, A., Brunt, K., Felikson, D., Fricker, H., Hawley, B., Hofton, M., Luthcke, S. Pie, N., Schutz, B., Shuman, C., Yi, D., and Zwally, J.: Summary of ICESat-1 inter-campaign ele-

TCD
7, 4287–4319, 2013

vation biases and detection methods, Fall Meeting, AGU, San Francisco, CA, 3–7 December 2012.

Zwally, H. J., Schutz, B. E., Abdalati, W., Abshire, J. B., Bentley, C. R., Brenner, A. C., Bufton, J. L., Dezio, J.,Hancock, D., Harding, D. J., Herring, T. A., Minster, J. B., Quinn, K., Palm, S., Spinhirne, J. D., and Thomas, R. H.: ICESat's laser measurements of polar ice, atmosphere, ocean and land, J. Geodyn., 34, 405–445, doi:10.1016/S0264-3707(02)00042-X, 2002.

Zwally, H. J., Li, J., Brenner, A. C., Beckley, M., Cornejo, H. G., DiMarzio, J., Giovinetto, M. B., Neumann, T. A., Robbins, J., Saba, J. L., Yi, D., and Wang, W.: Greenland ice sheet mass balance: distribution of increased mass loss with climate warming; 2003-07 vs. 1992–02, J. Glaciol., 57, 88–102, doi:10.3189/002214311795306682, 2011.

TCD
7, 4287–4319, 2013

Table 1. ICESat campaign metadata and G-C offset statistics. Campaigns are listed sequentially in time and are named as described in the text. Laser 2 campaigns are shown in bold to highlight the switching that occurs between lasers during the mission. The valid returns column gives the percentage of shots for which a surface elevation was recorded, which tends to drop as laser energy decreases.

Campaign	Start Date	End Date	# Days	% Valid Returns	# Valid Returns	G-C Mean (cm)	G-C σ (cm)
L1a/L1b	2/20/03	3/29/03	37	73 %	85 862 366	1.77	1.99
L2a	**10/13/03**	**11/19/03**	**37**	**63 %**	**80 770 785**	**5.90**	**1.83**
L2b	**2/17/04**	**3/21/04**	**33**	**64 %**	**72 697 059**	**0.60**	**2.07**
L2c	**5/18/04**	**6/21/04**	**34**	**53 %**	**62 361 334**	**−0.16**	**3.70**
L3a	10/3/04	11/8/04	36	64 %	79 437 302	−0.58	1.93
L3b	2/17/05	3/24/05	35	67 %	79 778 747	−1.37	1.95
L3c	5/20/05	6/23/05	34	65 %	75 890 428	−3.44	2.46
L3d	10/21/05	11/24/05	34	63 %	71 662 990	−4.06	2.56
L3e	2/22/06	3/28/06	34	65 %	74 789 938	−4.13	2.10
L3f	5/24/06	6/26/06	33	62 %	71 172 594	−3.72	2.27
L3g	10/25/06	11/27/06	33	61 %	70 179 600	−4.07	2.45
L3h	3/12/07	4/14/07	33	63 %	73 058 093	−3.93	2.23
L3i	10/2/07	11/5/07	34	59 %	68 161 111	−3.86	2.38
L3j	2/17/08	3/21/08	33	63 %	71 872 084	−3.91	2.57
L3k	10/4/08	10/19/08	15	59 %	29 447 798	−4.13	2.66
L2d	**11/25/08**	**12/17/08**	**22**	**54 %**	**40 865 517**	**−0.11**	**5.36**
L2e	**3/9/09**	**4/11/09**	**33**	**39 %**	**44 606 427**	**2.65**	**8.79**
L2f	**9/30/09**	**10/11/09**	**11**	**35 %**	**12 844 976**	**1.69**	**7.03**
Laser 1 avg				73 %		1.77	1.99
Laser 2 avg				51 %		1.76	4.80
Laser 3 avg				63 %		−3.38	2.32
Average All				60 %		−1.38	3.13

TCD
7, 4287–4319, 2013

Table 2. G-C offset trend estimates (and formal 1-sigma errors) using different data periods and different least-squares weighting applied to each campaign. Trend A uses inverse-variance weighting derived from the G-C offset statistics in Table 1, Trend B uses uniform weighting, and Trend C uses weights derived from global ICESat sampling by campaign. These trend estimates also represent the impact of the G-C correction on dh/dt, indicating that all ICESat-derived ice elevation change estimates should become more negative once the G-C offset is removed.

Begin Campaign	End Campaign	G-C Trend A (cm yr^{-1})	G-C Trend B (cm yr^{-1})	G-C Trend C (cm yr^{-1})
L2a	L3i	-2.13 ± 0.53	-1.90 ± 0.48	-1.90 ± 0.51
L2a	L3j	-1.88 ± 0.47	-1.62 ± 0.41	-1.76 ± 0.47
L2a	L3k	-1.64 ± 0.41	-1.39 ± 0.36	-1.55 ± 0.42
L2a	L2d	-1.54 ± 0.40	-1.00 ± 0.32	-1.17 ± 0.38
L2a	L2e	-1.48 ± 0.40	-0.62 ± 0.29	-1.05 ± 0.37
L2a	L2f	-1.38 ± 0.40	-0.36 ± 0.26	-0.92 ± 0.36

TCD
7, 4287–4319, 2013

Table 3. ICESat sampling of the Ross and Filchner-Ronne ice shelves for the elevation trend estimates in Sect. 3.4. We list the number of shots used by campaign over the entire ice sheet (S_i in Eq. A11), as well as the relative campaign sampling weights (expressed as a percentage of the maximum number of shots on that ice shelf for any campaign). There are large differences in relative campaign sampling between the two ice shelves for L2a, L3g and L3j, which results in different estimates for the elevation trend impact of the G-C offset.

Campaign	Ross		Filchner-Ronne	
	# Shots Used	% Max	# Shots Used	% Max
L2a	395 218	96	179 955	68
L2b	285 648	69	198 316	75
L2c	378 640	92	244 073	92
L3a	377 854	91	245 864	93
L3b	335 248	81	202 618	77
L3c	363 814	88	264 081	100
L3d	358 902	87	197 763	75
L3e	291 486	71	151 919	58
L3f	368 413	89	234 540	89
L3g	413 425	100	169 199	64
L3h	329 989	80	227 046	86
L3i	384 517	93	235 922	89
L3j	262 832	64	220 324	83
L3k	160 299	39	127 620	48
L2d	189 205	46	123 881	47
L2e	261 577	63	190 585	72
L2f	104 189	25	49 165	19

TCD
7, 4287–4319, 2013

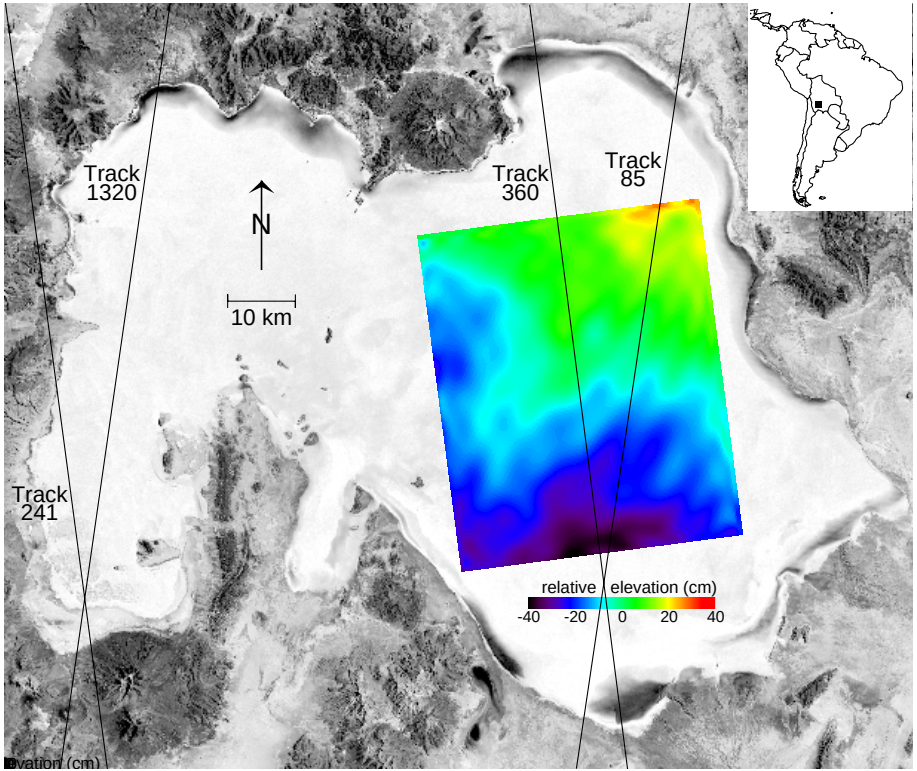

Fig. 1. The reference DEM used in this study, located on the salar de Uyuni in Bolivia. Topographic relief across the 45-by-54 km DEM is only 80 cm, making this region of the salar one of the flattest natural surfaces on Earth. ICESat tracks 85 (descending) and 360 (ascending) cross the DEM and are used for range validation.

TCD
7, 4287–4319, 2013

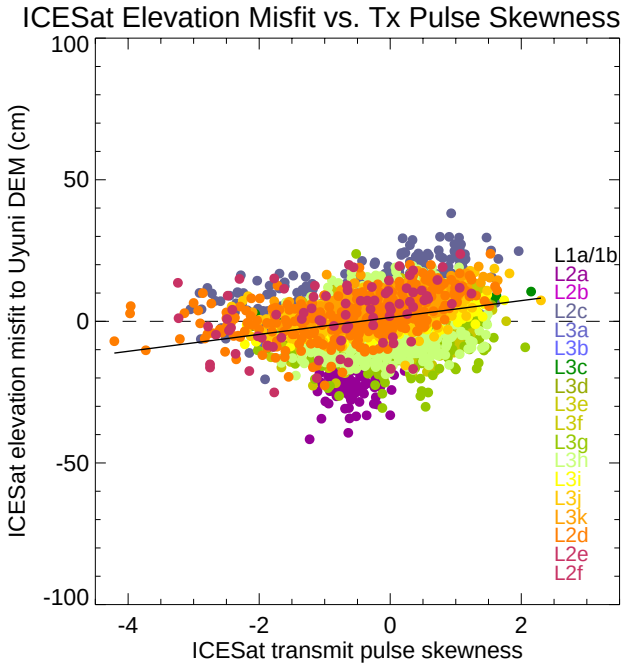

Fig. 2. Scatterplot of ICESat elevation misfits versus the transmit pulse skewness for each shot, with the linear correlation between the two indicated by the black line. The Pearson correlation coefficient *R* is 0.30 for the whole dataset, with higher coefficients for most of the individual campaigns – up to 0.64 for L2b and L3c (see campaign color code at right of plot).

TCD
7, 4287–4319, 2013

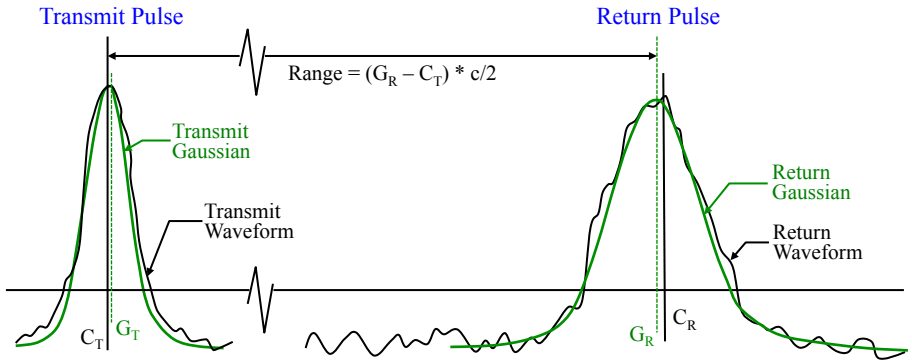

Fig. 3. ICESat range determination illustration, adapted from Brenner et al. (2003). The transmit and return waveforms are shown in black, and the Gaussian fits to those waveforms are shown in green. The centroids of the transmit (C_T) and return (C_R) waveforms are indicated by the solid black vertical lines, and the peak locations of the Gaussian fits to the transmit (G_T) and return (G_R) waveforms are indicated by the dotted green vertical lines. The ICESat range determination algorithm that was implemented through data release R633 used the time difference between the return Gaussian peak and the centroid of the transmit waveform (multiplied by the speed of light c and divided by 2 to get one-way range), which introduces a range error equal to $(G_T - C_T) \cdot c/2$.

TCD
7, 4287–4319, 2013

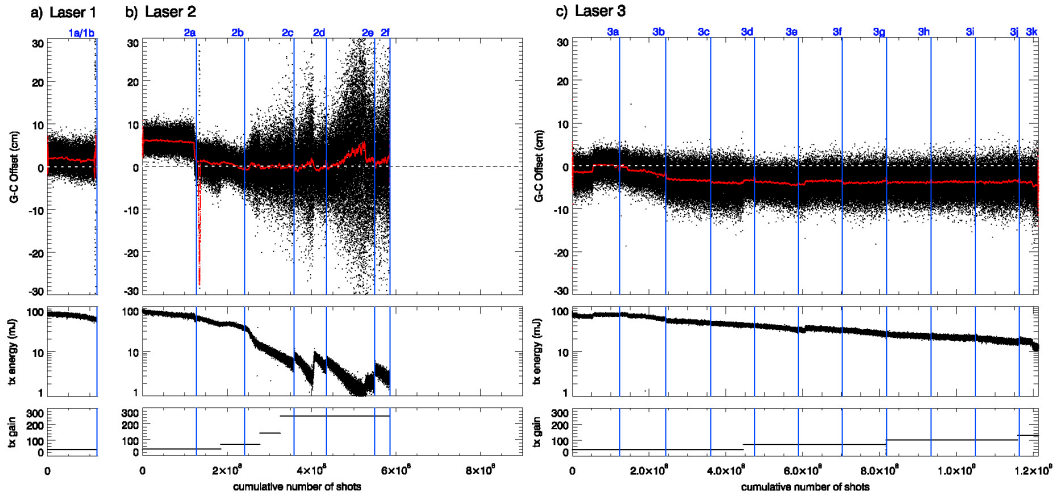

Fig. 4. The G-C offset, transmit energy, and transmit gain for Laser 1 **(a)**, Laser 2 **(b)**, and Laser 3 **(c)**, ordered sequentially by cumulative number of shots for each laser. The red line in the top plot is the 10 000-shot moving average of the G-C offset. ICESat campaigns are named in blue at the top of the plots and are delineated by blue lines marking the end of each campaign period. The scatter in the G-C offset grows as transmit energy drops, especially below 20 mJ.

TCD
7, 4287–4319, 2013

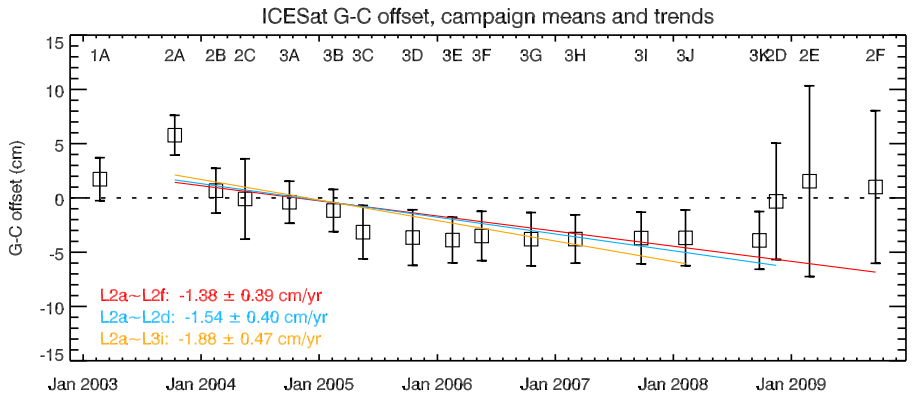

Fig. 5. G-C offset campaign means and trend estimates for selected data spans from Table 2, Trend A. The boxes are the mean values for each campaign of the G-C offset data in Fig. 4, the error bars are the offset standard deviations for each campaign, and the different lines are G-C offset trends estimated for different data periods using inverse-variance weighting. The G-C offset has a bigger impact on elevation trends when campaigns at the end of the mission are excluded.

TCD
7, 4287–4319, 2013

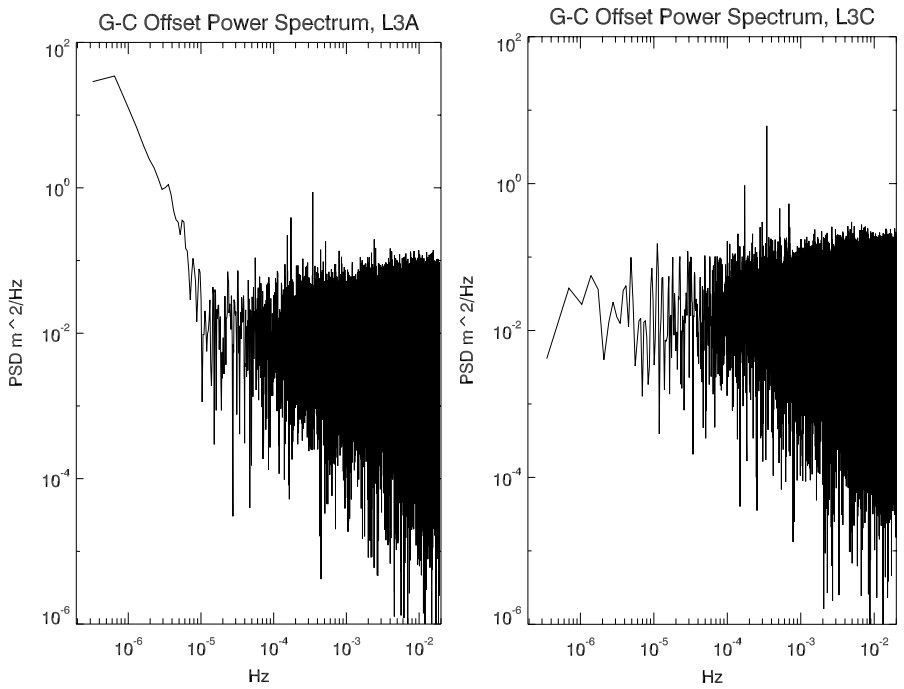

Fig. 6. Power spectrum of G-C offset for campaigns L3a (left) and L3c (right), showing a flat spectrum beyond 10^{-5} Hz and different behavior at lower frequencies. The main difference between the two campaigns is that the moving average of the G-C offset jumps abruptly in L3a while it is flat in L3c (see Fig. 4c).

TCD
7, 4287–4319, 2013